Observing Seasonal Variabilities of a Permafrost Landscape With PolSAR, InSAR and Pol-InSAR

Paloma Saporta, Alberto Alonso-González, *Member, IEEE*, Jennika Hammar, Inge Grünberg, Julia Boike, and Irena Hajnsek, *Fellow, IEEE*

***Abstract*—Synthetic aperture radar (SAR) remote sensing is an established approach for observing Earth processes. The combination of different types of SAR acquisitions in polarimetric, interferometric, and polarimetric-interferometric frameworks is well studied for retrieving parameters of certain landscape features, such as forests and glaciers. These frameworks have only been rarely applied to permafrost regions, characterized by particular dielectric and structural properties, in particular frozen ground. Here, we investigate the effect of permafrost characteristics on the different SAR imaging modes. This study performs an analysis of the SAR data retrieved during an airborne campaign conducted by the German Aerospace Center (DLR) in the Canadian low Arctic. Established polarimetric SAR, SAR interferometry, and polarimetric SAR interferometry techniques are applied on the region of interest. For each of these techniques, results are analyzed in several dimensions. Winter and summer observables are compared, the influence of vegetation type is assessed, and differences between results obtained at different radar frequencies are shown. This study leads the path toward the retrieval of soil and vegetation parameters in permafrost tundra environments using multimodal SAR techniques.**

***Index Terms*—Airborne synthetic aperture radar (SAR), frozen soil, SAR Interferometry (InSAR), penetration, permafrost, polarimetric SAR interferometry (Pol-InSAR), polarimetric SAR (PolSAR), synthetic aperture radar.**

I. Introduction

REMOTE Sensing from airborne and spaceborne platforms has the capability to provide large and continuous spatial coverage of remote regions around the globe and is therefore ideal for permafrost studies [1], [2]. In particular, Arctic permafrost regions have gained increasing attention in the context of global change and rising air temperatures. While permafrost thaw has the potential to release large amounts of previously frozen organic carbon, contributing to greenhouse gas emissions, there remain significant uncertainties about the timing, magnitude, and overall climate impact [3], [4], [5]. This makes the monitoring of Arctic permafrost state a critical topic.

Permafrost is defined as material that remains below 0°C for at least two consecutive years. Permafrost landscapes are typically covered by a layer of snow during winter, while in summer they are characterized by a seasonal upper layer, known as the active layer, which thaws and refreezes annually. Vegetation plays a crucial role as a surface cover and buffer, influencing heat exchange between the subsurface and the atmosphere [6]. The presence of vegetation, along with snow cover, leads to significant variations in surface properties, as the dielectric properties of the surface alter with the freezing and thawing cycles, influencing how it interacts with radar and other remote sensing techniques [7], [8]. Furthermore, as the porebound water within the active layer undergoes seasonal phase transitions between water ice and liquid water, the associated reduction of the effective pore space volume of this water as it melts translates into seasonal subsidence of the ground surface, while the increase of this water volume as it freezes leads to seasonal heaving of the ground surface [9].

As permafrost is characterized by the thermal state of the soil subsurface, most remote sensing techniques can only infer its properties indirectly. This typically includes monitoring aboveground features, such as snow and vegetation characteristics, or surface features like freeze/thaw cycles and surface deformation at seasonal and long-term time scales. Synthetic aperture radar (SAR) is a valuable technique for permafrost monitoring in several aspects. The radar signal is sensitive to changes in soil moisture and dielectric properties, allowing for the spatial and temporal mapping of freeze/thaw transitions [10]. SAR imagery is also sensitive to the landscape structure (topography, distribution of scatterers in height), as well as the type and orientation of the individual scatterers in this landscape [11], [12]. Finally, SAR has the advantage of operating almost independently of weather conditions, unlike optical sensors, making it reliable for year-round data collection. In the past years, different target parameters that are characteristic for permafrost have been investigated using various techniques, as detailed in [1], [2]. Radar backscatter is used to detect and map the freeze/thaw status of the

Received 11 October 2024; revised 23 January 2025; accepted 3 March 2025. Date of publication 14 March 2025; date of current version 29 April 2025. This work was supported by Helmholtz Imaging Platform through the Hidden Image of Thawing (HIT) Permafrost Project. *(Corresponding author: Paloma Saporta.)*

Paloma Saporta and Irena Hajnsek are with the Polarimetric SAR Interferometry Research Group, Microwaves and Radar Institute (HR), German Aerospace Center (DLR), 82234 Wessling, Germany, and also with the Institute of Environmental Engineering (IFU), Swiss Federal Institute of Technology (ETH) Zurich, 8092 Zurich, Switzerland (e-mail: paloma.saporta@dlr.de; irena.hajnsek@dlr.de).

Alberto Alonso-González is with the Signal Theory and Communications Department, Universitat Politècnica de Catalunya, 08034 Barcelona, Spain.

Jennika Hammar and Inge Grünberg are with the Permafrost Research Group, Alfred Wegener Institute Helmholtz Centre for Polar and Marine Research, 14473 Potsdam, Germany.

Julia Boike is with the Permafrost Research Group, Alfred Wegener Institute Helmholtz Centre for Polar and Marine Research, 14473 Potsdam, Germany, and also with the Geography Department, Humboldt-Universität zu Berlin, 10117 Berlin, Germany.

Digital Object Identifier 10.1109/JSTARS.2025.3551422

soil, both spatially and temporally. Indeed, the freezing of wet soils induces a decrease of its liquid water content and therefore of its relative permittivity, leading to a drop in radar backscatter of several dB [7]. This characteristic allows the mapping of surface freeze–thaw cycles by detecting a substantial decrease in SAR backscatter within a season [8]. Different studies focused on the estimation of the seasonal freeze/thaw transition date [13] or emphasized the modeling of the seasonal backscatter thresholds [14]. At larger wavelengths, the combination of a multilayer model with backscatter observations was used to estimate the active layer thickness and the soil dielectric profile from P-band airborne data [15].

In addition, polarimetric SAR (PolSAR) studies associated the frozen and thawed conditions of the landscape with variations in polarimetric descriptors, which reflect different scattering mechanisms. Investigations included eigenvector-based decomposition (entropy/alpha approach in [16], [17]) or model-based decomposition (Freeman–Durden approach in [18]).

Repeat-pass differential SAR interferometry (DInSAR) recently became a popular tool to monitor elevation changes related to heaving and subsidence of the active layer in permafrost areas [19], [20]. Associated with a ground model, the DInSAR derived seasonal subsidence has been related to the active layer thickness [21], [22]. Excess ground ice at the top of the permafrost has been identified from late-season subsidence detected with DInSAR [23], [24]. Long-term deformation trends retrieved from multiannual DInSAR have been associated with permafrost degradation [25], [26]. While the differential interferometric signal related to soil deformation is of interest and is studied in several research groups [21], [22], [23], [25], [26], [27], [28], [29], there is currently no study investigating the SAR interferometry (InSAR) observables derived from a short term cross-track spatial baseline.

In the past years, remote sensing of permafrost studies have been relying on data from SAR systems operating at various frequencies, mostly at X-band (TerraSAR-X), C-band (ERS, Radarsat-2, Sentinel-1) and L-band (ALOS). Only a limited number of studies consider combining SAR data at several frequencies. Part of these studies computed estimates at each frequency individually and compared them at a later stage. This includes comparing scattering characteristics at X-, C-, and L-band in [30], and at C- and L-band in [31], as well as estimating seasonal subsidence at X- and C-band in [29] and [28], and X-, C-, and L-band in [20]. Only two studies combined the SAR data early on in a model to estimate the final output. In [32], X- and C-band polarimetric data was combined to produce a landcover classification over Richards Island, Canada. In [33], airborne L-band DInSAR and P-band PolSAR parameters were used to estimate active layer thickness and a soil moisture profile for several sites in Alaska and Canada. Most of these studies were based on satellite data, with sensors onboard of different platforms. Combining such data faces the challenges of different observation periods and of the different acquisition geometries (incidence angle, spatial resolution). These issues can be circumvented by using an airborne dataset where all frequencies are acquired simultaneously, as proposed in this paper. The multifrequency dimension investigated in this study adds another innovative aspect.

TABLE I
TYPICAL VEGETATION HEIGHT FOR THE DIFFERENT VEGETATION TYPES AT TVC

Vegetation type	Vegetation height
Lichen	3 cm to 25 cm
Moss	3 cm to 40 cm
Dry hummock	8 cm to 35 cm
Tussock	8 cm to 35 cm
Dwarf shrub	20 cm to 40 cm
Single shrub	40 cm to 100 cm
Riparian shrub	100 cm to 250 cm
Tree	200 cm to 1000 cm

In this article, we propose a comprehensive polarimetric, interferometric, and polarimetric–interferometric analysis at several frequencies of a selected test site, imaged under successive frozen and thawed conditions.

The rest of this article is organized as follows. The SAR and airborne laser scanning (ALS) datasets used throughout this article are described in the Section II. The different investigation methods are presented in Section III, ranging from established polarimetric techniques [entropy/alpha, copolar phase differences (CPD) and polarimetric change analysis] in Section III-A, to interferometric coherence and polarimetric SAR interferometry (Pol-InSAR) coherence region parameters in Sections III-B and III-C, respectively. The results are analyzed in Section IV, with a particular attention to the variations of the observables with SAR frequency (X-, C-, and L-band), season (summer and winter), and vegetation type.

II. DATA

This section describes the test site and the different remote sensing data that was used in this article. The dataset consisted of two sources: the airborne SAR dataset (see Section II-A) and the ALS dataset (see Section II-B).

Both datasets were acquired over a test-site located in the Trail Valley Creek catchment (TVC) in the Northwest Territories, Canada (68.7°N, 133.5°W). This site belongs to the continuous permafrost zone at the transition between boreal forest and tundra, with permafrost reaching 100 to 150 m thickness [34], [35]. The site features gently rolling hills covered by low-shrub tundra vegetation and some isolated trees. Grünberg et al. [36] described in details the different vegetation types at TVC. Table I shows the typical vegetation height for the vegetation types that are most relevant in this study.

Thirty years of climate records in Inuvik, covering the 1991–2020 period, indicate an average air temperature of −7°C and an average of 250 mm total precipitation (snow and rainfall) per year [37]. In winter, the ground and the vegetation are predominantly frozen, and covered with snow. In summer, the active layer depth varies spatially between a few decimeters and about 1 m across the site. The active layer is completely below zero degrees in winter. The choice of the TVC test site was motivated by the manifold ground measurements and studies led by various

TABLE II
SUMMARY OF SAR PARAMETERS

band	frequency	polarisations	range resolution	azimuth resolution	summer flight	winter flight	Baseline	k_z
X	9.7 GHz	fully polarimetric	97 cm	50 cm	15/08/2018	23/03/2019	15 m	1 rad/m
C	5.3 GHz	fully polarimetric	97 cm	50 cm	15/08/2018	23/03/2019	25 m	1 rad/m
L	1.3 GHz	fully polarimetric	1.3 m	60 cm	15/08/2018	23/03/2019	100 m	1 rad/m

research institutions, which have already established TVC as a important location for permafrost research. Investigation topics include hydrology [31], [38], snow properties [39], [40], [41], greenhouse gas fluxes [42], vegetation [43] and the link between these parameters and permafrost characteristics [36], [44].

A. Multifrequency Pol-InSAR Dataset

This article is based on the airborne SAR dataset acquired by the DLR's F-SAR sensor in the frame of the Permafrost Airborne SAR campaign in summer 2018 and winter 2019 [45]. The campaign aimed at investigating the interaction between frozen soils and radar waves with various characteristics. Several sites were imaged in Canada in order to cover a North–South gradient corresponding to the transition between arctic tundra and continuous permafrost landscapes in the North to boreal forests over discontinuous permafrost in the South. In this article, we considered the northernmost site, which covers the TVC catchment. Over a scene of approximately 14 km by 5 km, DLR's F-SAR sensor was operated at X-, C-, and L-band, with respective wavelengths of 3.1 cm, 5.7 cm and 22.6 cm. Fully polarimetric data was acquired and tracks with several spatial baselines were flown within one day, allowing to form a polarimetric SAR interferometric dataset. The SAR data was processed and calibrated at the German Aerospace Center [46]. Specifically, the data considered in this study has following parameters, as summarized in Table II.

1) Frequency: X-, C-, and L-band.
2) Polarimetry: The acquisitions were fully polarimetric (HH, VV, HV, VH).
3) Interferometry: At each frequency, we built single-baseline interferograms to form an InSAR and a Pol-InSAR dataset. For each pair, the spatial baseline was chosen such that the vertical wavenumber is similar in between frequencies (see Table II). The temporal baseline associated with each pair is shorter than 2 h for L-band, shorter than 1 h for C-band and approximately half an hour for X-band.
4) Spatial resolution: Submeter for all frequencies (see Table II for details).
5) Season: We considered both the summer dataset (acquired in August 2018) and the winter dataset (acquired in March 2019).
6) Zone: We considered a smaller region of interest (ROI) within the SAR footprint, covering the Trail Valley Creek Research station and Siksik Creek.
7) Weather conditions: Hourly records at the Trail Valley meteorological station indicated little to no rain (maximum 1 mm) on the days before the summer flight, suggesting dry conditions. For the winter dataset, we assume dry snow conditions based on the study in [47], which confirmed the absence of liquid water in the snowpack during the F-SAR flight (23rd of March 2019). In addition, air temperatures remained consistently below $-5.8°$C before and during the overflight.

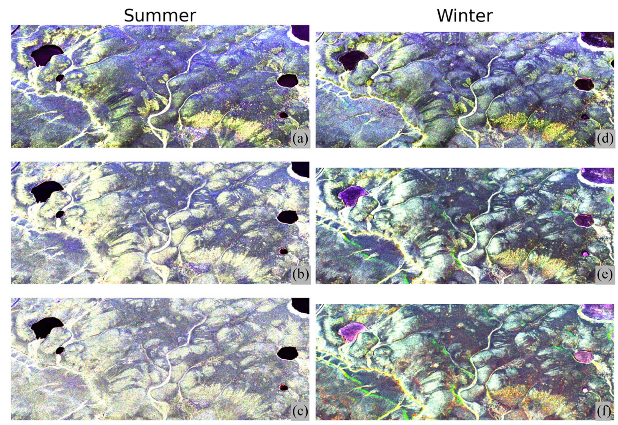

Fig. 1. Pauli representation of the ROI within the radar footprint. The left column contains the summer acquisitions at (a) L-band, (b) C-band, and (c) X-band. The right column contains the winter acquisitions at (d) L-band, (e) C-band, and (f) X-band. The Pauli RGB scale takes HH-VV intensity in the red channel, HV + VH intensity in the green channel and HH + VV intensity in the blue channel. Each of the six Pauli images is scaled individually.

The polarimetric Pauli representations provide a first qualitative description of the type of scattering occurring inside the scene, and are obtained by arranging the four possible polarimetric channel combinations into relevant linear combinations. The Pauli images over the ROI, in summer and winter, and for each frequency, are represented on Fig. 1. RGB Pauli images can be understood as such: blue (HH+VV) is associated with surface scattering, red (HH-VV) with dihedral scattering and occurring typically at ground-trunk interfaces, and green (HV+VH) corresponds to volume scattering, typically coming from multiple scattering interactions within the vegetation. Note that each Pauli image has been scaled individually, therefore the intensity of these scattering mechanisms are to be understood relatively to each other, within one scene.

On Fig. 1, the summer scenes indicate a strong contrast between the lakes, and the land and vegetated areas. The lakes appear black, indicating low backscatter. The areas with short vegetation appear in blue–gray indicating rough surfaces, while areas with taller vegetation (trees, streams with riparian shrubs) appear brighter. Larger wavelengths exhibit larger contrast within the scene. In winter, the lakes are frozen and appear bright as scattering occurs in the ice. The land appears, like in summer, as rough surface and exhibits a combination of scattering mechanisms. All wavelengths show a stronger contrast within the scene in winter compared to the summer Pauli representations. Green

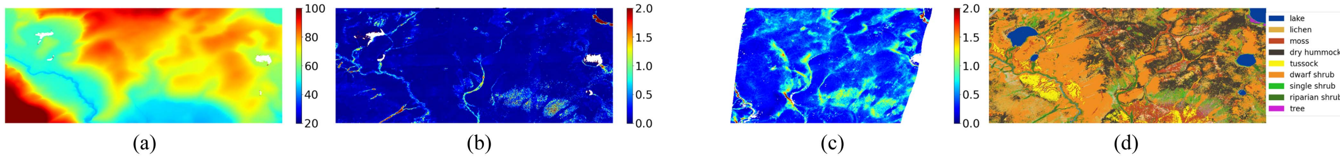

Fig. 2. Datasets derived from the ALS survey have been transferred into the radar geometry and restricted to the ROI. From left to right, the maps are following: (a) DTM [48], (b) vegetation height [48], (c) snow depth [50], and (d) vegetation classification. Only the vegetation types that are considered in this article are shown in the legend of the vegetation classification. Invalid points have been masked out and appear in white in (a)–(c).

stripes at C- and X-band correspond to areas with deeper snow accumulating at the back of slopes.

B. Airborne Laser Scanning Dataset

In parallel with the summer 2018 airborne SAR data acquisition, the Alfred Wegener Institute (AWI) conducted an ALS survey at the TVC site on the 20th August 2018. A digital terrain model (DTM) and vegetation height map were derived from the waveform analysis [48]. We reprocessed the ALS point cloud of summer 2018 with the same methodology in a bigger spatial extent to cover the complete SAR footprint. In addition, we implemented a refined methodology based on the approach described in [49] to create a high-resolution vegetation classification map for the SAR footprint. Unlike the previous version, which combined ALS products with 10 m resolution RGB orthophotos, the updated map was generated exclusively using ALS-derived data. The methodology was enhanced by incorporating additional variables, such as amplitude and echo width, along with previously utilized data like the DTM and vegetation height. The updated classification improved spatial resolution from 10 m to 1 m, resulting in significantly increased detail and accuracy. Additional ALS acquisitions were performed during the winter season, on the 10th April 2019, and a snow depth map was derived from the elevation difference between the snow-free and the snow-covered DTMs [50], [51]. The snow map covers a transect of the whole SAR footprint, and a large part of the ROI as can be seen on Fig. 2. All maps are derived at 1 m $\times$ 1 m resolution, and are backgeocoded into the geometry of the radar scene. The DTM was used as reference topography for the SAR processing. The DTM, the vegetation height map, the vegetation map and the winter snow map were used in this article to support the radar analysis and the interpretation of the results. Fig. 2 represents these datasets in the radar geometry over the ROI, covering the same area and geometry shown in Fig. 1.

III. Methods

The following section describes the methods used to investigate the SAR dataset in conjunction with the ALS products.

A. SAR Polarimetry

Several established polarimetric techniques were investigated to evaluate the scattering over the scene.

1) Entropy/ Alpha: Entropy/ alpha angle decomposition is a common polarimetric method based on the eigenvectors of the polarimetric coherency matrix, which is derived from the fully polarimetric acquisitions in the Pauli basis. As described in [12], the entropy H corresponds to the randomness of the scattering process at the given pixel, while the mean alpha angle $\bar{\alpha}$ represents the mean type of scattering mechanism. Low entropy values (close to 0) indicate a single type of scattering mechanism, while larger entropy values (close to 1) correspond to a larger number of significant scatterers. The mean alpha angle varies between 0° and 90°. Small $\bar{\alpha}$ values, around the lower limit 0°, indicate surface scattering, while larger $\bar{\alpha}$ values, and at maximum 90°, are characteristic for dihedral scattering. Intermediate values (40° to 50° [12]) associated with high entropy values correspond to the scattering produced by a volume of scatterers, for instance the multiple scattering within a heterogeneous medium such as vegetation.

2) Copolar Phase Differences: The propagation of radar waves in an anisotropic medium, such as snow can result in a polarisation-dependent polarization speed, leading to a phase difference between HH and VV images. The work in [52] and [53], for instance, related these copolar phase differences (CPD) at L-band and X-band, respectively, to the dielectric constant of the snow along different directions (which depend on the snow density and the anisotropy of the snow grains), the snow depth and the radar parameters (incidence angle, radar wavelength). CPD from propagation into snow increase in absolute value for increasing local incidence angle, affecting their interpretation, in particular in slopes where the snow accumulates because of strong winds. We computed the CPD, as $\Phi_c = \Phi_{HH} - \Phi_{VV}$, and compared it qualitatively with the snow depth derived from the ALS dataset.

3) Change Analysis: The polarimetric change analysis method we considered was originally developed for agriculture and crop growth monitoring [54]. This method retrieves the type and amount of change between the two fully polarimetric SAR images to be compared by maximizing the polarimetric contrast measure between the two images. Note that this method takes as input two coherency matrices to be compared. In our case, we computed them (1) from fully polarimetric single look complex images (SLC) at two different seasons and (2) from the coherency matrices averaged over all the pixels of a certain vegetation class. The optimization reduces to a generalized eigendecomposition problem, where the generalized eigenvalues λ_1, λ_2, and λ_3 correspond to the maximum, intermediate, and minimum polarimetric contrast. The eigenvectors $\mathbf{w_1}$, $\mathbf{w_2}$, and $\mathbf{w_3}$ correspond to the polarizationstates associated with the eigenvalues. If the coherency matrices to be compared are defined in the Pauli basis, the eigenvectors $\mathbf{w_i}$ are as well and they can be related to physical scattering mechanisms. Furthermore, the eigenvalues indicate the direction of change between both images: eigenvalues larger than 1 indicate an increase in backscattered power, while eigenvalues smaller than 1 indicate a decrease in backscattered power. Alonso-González et al. [54] defines two indicators p_{inc} and p_{dec} that represent the change information in an aggregated way by weighting the optimized polarization states by their associated change intensity

$$\mathbf{p}_{\text{inc}} = \left[\sum_{i|\lambda_i > 1}^{]} (10log_{10}\lambda_i)^2 \cdot \mathbf{w_i w_i^*} \right]^{1/2} \tag{1}$$

$$\mathbf{p}_{\text{dec}} = \left[\sum_{i|\lambda_i < 1}^{]} (-10log_{10}\lambda_i)^2 \cdot \mathbf{w_i w_i^*} \right]^{1/2}. \tag{2}$$

In (1), the logarithmic term with λ_i represents the intensity of the change in dB. $\mathbf{w_i w_i}^*$ refers to the elementwise product of the eigenvector, which captures the influence of the polarization state. p_{inc} and p_{dec} integrate the information on the amount of change by their intensity and the type of change by their color when represented as RGB.

B. SAR Interferometry

InSAR adds sensitivity to the distribution of scatterers in the vertical dimension. In the tundra permafrost case, this is particularly interesting as potential scattering or propagation within the frozen soil volume (winter case) could potentially be detected as volume decorrelation or as a negative phase center height with respect to the ground. Generally, heterogeneties or larger penetration depths possibly indicate the presence of ground ice, which is a critical parameter of permafrost landscapes, corresponding to potential locations of future ground degradation. In order to achieve this, penetration into the frozen ground from SAR must first be observed. As information about the distribution of scatterers in height is contained both in the norm and in the phase of the interferometric coherence, we considered complex interferometric coherences, computed from single baseline pairs.

1) Interferometric Coherence: The interferometric complex coherence is estimated starting from two coregistered SLC images. The total complex coherence can be expressed as the product of several contributions [11], [55], [56]

$$\gamma = \gamma_{\text{baseline}} \cdot \gamma_{\text{SNR}} \cdot \gamma_{\text{temporal}} \cdot \gamma_{\text{vol}}. \tag{3}$$

In (3), γ_{baseline} is the baseline decorrelation, γ_{SNR} the thermal noise decorrelation, γ_{temporal} the temporal decorrelation, and γ_{vol} the volume decorrelation. The volume decorrelation γ_{vol} accounts for the structure of the scatterers in the height direction, which includes penetration into natural volumes. γ_{vol} is the only complex parameter of (3) and is defined according to

$$\gamma_{\text{vol}} = e^{i\phi_0} \frac{\int_{z_{\text{min}}}^{z_{\text{max}}} f(z) e^{ik_z z}\, dz}{\int_{z_{\text{min}}}^{z_{\text{max}}} f(z)\, dz}. \tag{4}$$

In (3), ϕ_0 is the reference phase associated with the origin of the vertical z-axis, and $f(z)$, the vertical reflectivity profile, depends on the distribution of scatterers along the vertical axis and is defined between z_{min} and z_{max}. The vertical wavenumber, denoted by k_z, is a term depending both on the geometry of the acquisition and the radar signal

$$k_z = \frac{4\pi}{\lambda} \frac{\Delta\theta}{\sin(\theta)} \tag{5}$$

where θ is the incidence angle, $\Delta\theta$ is the difference of incidence angle between two acquisitions, and λ is the radar wavelength. The vertical wavenumber drives the vertical sensitivity of an interferometric pair.

As γ_{vol} is the variable of interest, various corrections were performed on the estimated interferometric complex coherence in order to isolate this parameter.

1) Baseline decorrelation was not negligible for our choice of baselines. We therefore performed range spectral filtering with range blocks: for each block, we selected the overlapping part of the range spectrum of each SLC. The flat Earth phase (i.e., the phase caused by the varying distance between each pixel and the sensor, which increases from near to far range) and the topographic phase were compensated during the range spectral filtering process [57]. After this step, the baseline decorrelation term was expected to be 1.
2) The coherence loss due to thermal noise decorrelation is given by

$$\gamma_{\text{SNR}} = \frac{1}{1 + \text{SNR}^{-1}} \tag{6}$$

where SNR is the signal-to-noise ratio, computed from the noise-equivalent sigma zero provided by the system.
3) The temporal decorrelation was deemed negligible within the time in between the two flights given the temporal baselines described in Section II-A, i.e.,: $\gamma_{\text{temporal}} \approx 1$.

The coherence retrieved after these corrections will be called a "corrected coherence" γ_{corr} in this article, and it should entail mostly contribution from γ_{vol}.

2) Interferometric Phase: After flat Earth phase and topographic phase correction, the interferometric phase indicates the phase center height at each pixel, which is a function of the vertical reflectivity profile only. Indeed, motion compensation was applied to account for the deviation of the airplane tracks from a straight light path, as these deviations can produce unwanted interferometric phases. This motion compensation procedure includes two steps (first order motion compensation, residual motion error compensation) that are described in [46]. These corrections were performed prior to this study. Since we assumed that the residual phase due to possible remaining baseline errors is changing slowly in the spatial domain, it was possible to calibrate the InSAR phases at L-band using a scatterer with known height and then relate the calibrated phases to a phase center height. We used a corner reflector, which was present on the scene for both summer and winter campaigns, as a phase reference and restricted the analysis of the calibrated InSAR phases to the vicinity of this corner reflector (a square of 800 m centered around the corner reflector). The corner reflector was installed on the ground, at a fixed height, and was not moved

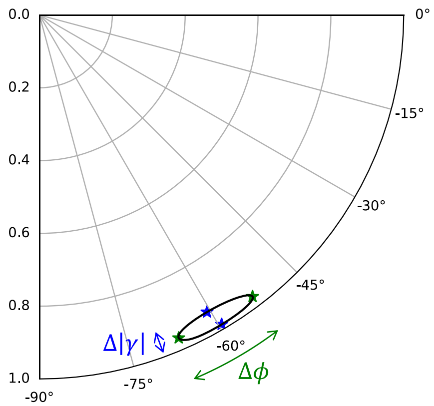

Fig. 3. Scheme of the Pol-InSAR coherence region at a single pixel. The black line is the shape of the coherence region. The extent in norm and phase are marked by the blue and green arrows, respectively.

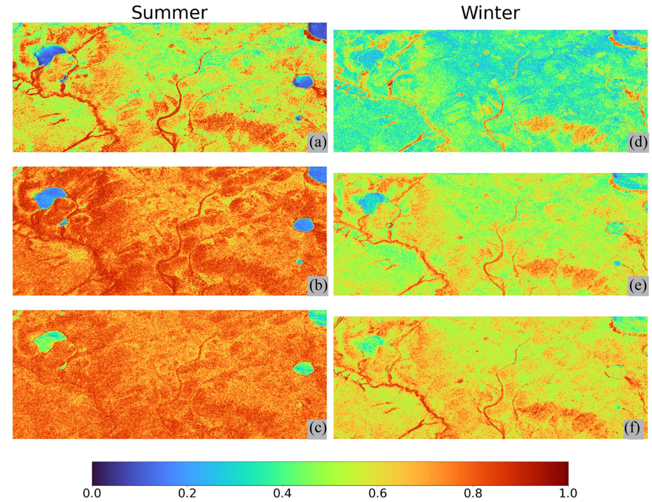

Fig. 4. Polarimetric entropy H (no unit). The left column contains H computed from the summer acquisitions at (a) L-band, (b) C-band, and (c) X-band. The right column contains H computed from the winter acquisitions at (d) L-band, (e) C-band, and (f) X-band.

between both campaigns. This analysis was only performed on the L-band data as the penetration of the radar wave into the frozen ground is expected to be deeper for larger wavelengths.

C. Polarimetric SAR Interferometry

In the Pol-InSAR framework, the concept of coherence region is a useful descriptor of the scattering inside the scene [58]. It consists in the representation, in the complex plane, of the set of interferometric coherences that can be retrieved for all the possible polarization $\mathbf{w}$. In particular, the Pol-InSAR coherence phase value at a given polarization is related to the phase center height for this polarization. Further on, considering several polarisation leads to the localisation of these phase center heights relatively to one another. The coherence region provides insights into the vertical distribution of scatterers for different scattering mechanisms.

Therefore, the shape of the coherence region, which depends on the scatterers in the considered pixel and the acquisition parameters, is a parameter of interest. The shape of the coherence region is characterized by the norm and the radial extent [59]. For example, in vegetated areas, the phase extent can reveal canopy height variations, while in icy landscapes, it can indicate subsurface scattering characteristics. The Pol-InSAR coherence region shape parameters are computed as follows. From the two fully-polarimetric scattering vectors in the Pauli basis at each end of the baseline, the individual coherency matrices T_{11} and T_{22} as well as the polarimetric interferometric matrix Ω_{12} are computed as described in [59]. Let us define the whitened matrix $\Pi = T_M^{-1/2}\Omega_{12}T_M^{-1/2}$ where $T_M = 1/2(T_{11} + T_{22})$. The whitening operation ensures that the coherence region can be expressed as the field of values of the matrix Π, which represents all possible coherence states across different polarizations, illustrating the scattering diversity within a pixel. The polarization states optimizing coherence norm and phase can be retrieved from the eigendecomposition of the elements of the polar decomposition of Π.

Fig. 3 presents a schematic of the coherence region and its shape characteristics: the norm extent $\Delta|\gamma|$ and the phase extent $\Delta\phi$. To account for the variations of the vertical wavenumber k_z within the zone of interest, we translated the phase extent into the associated height extent: $\Delta h = \Delta\phi/k_z$.

It has to be noted that the coherence region extent in phase is a relative measurement, independent from the absolute phase calibration. In our case, this allowed to retrieve information on the entire scene and not restrict the analysis spatially to the vicinity of the corner reflector.

IV. Data Analysis

For all methods described in the previous section, we analyzed the variability of the products in several dimensions as follows.

1) The three frequencies: X-, C-, and L-band.
2) Both seasons: summer and winter.
3) The most relevant vegetation classes.

A. SAR Polarimetry

1) Entropy/ Alpha: Plots of the scattering entropy and mean alpha angle are shown on Figs. 4 and 5. Fig. 6 combines the 2-D contour plots of the entropy with respect to the mean alpha angle for each vegetation type separately. The lines of the contour plots indicate a fixed density threshold, while the points correspond to the maximum of the density distribution.

For all bands, the scene presents lower H and $\bar{\alpha}$ values in winter compared to summer, which can be interpreted as a change from more volume-like scattering in summer to surface-like scattering in winter. This trend was already observed in previous studies, such as at C-band in [16] and [17]. In winter, the vegetation is mostly frozen and therefore it appears more transparent in term of scattering. This could explain the overall decrease of H and $\bar{\alpha}$.

The heterogeneities observed over the scene in Figs. 4 and 5 justify to consider vegetation types separately. Taking now into account the vegetation type, the 2-D contour plots of H /$\bar{\alpha}$ show various sensitivity depending on the frequency and season.

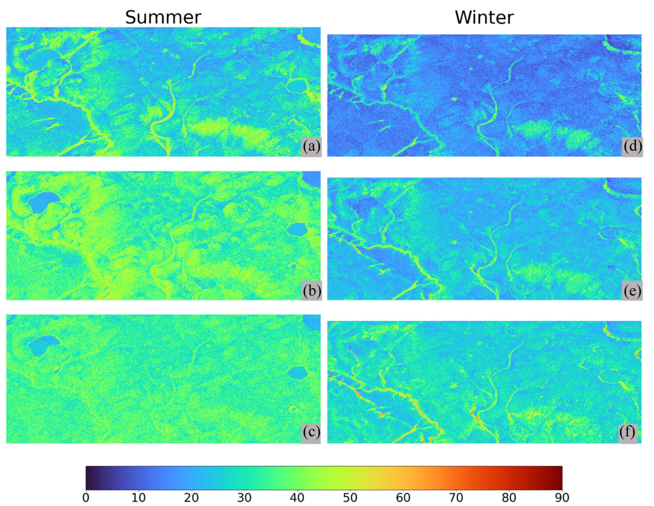

Fig. 5. Mean alpha angle $\bar{\alpha}$, in degrees. The left column contains $\bar{\alpha}$ computed from the summer acquisitions at (a) L-band, (b) C-band, and (c) X-band. The right column contains $\bar{\alpha}$ computed from the the winter acquisitions at (d) L-band, (e) C-band, and (f) X-band.

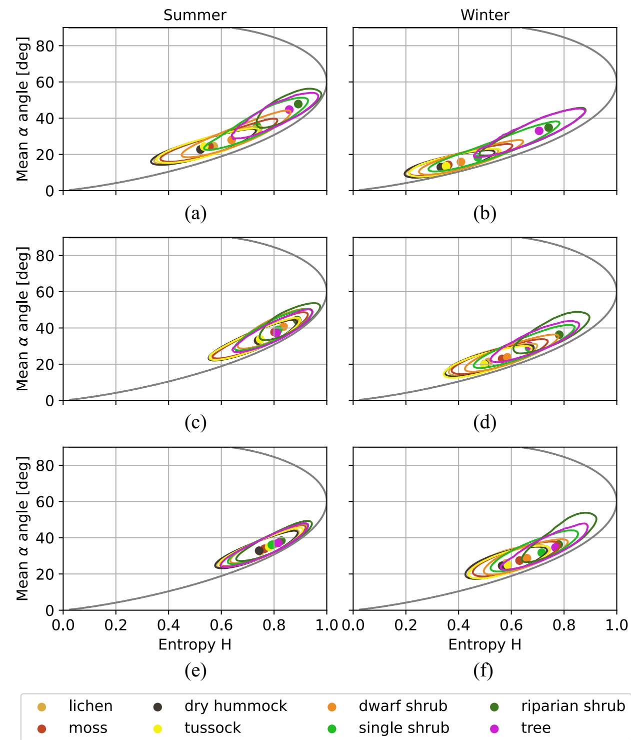

Fig. 6. 2-D $H/\bar{\alpha}$ distribution. The left and right columns contain the results in summer and winter respectively. (a), (d) Top, (b), (e) middle, (c), (f) and bottom rows correspond to L-, C-, and X-band, respectively. The lines represent contour plots at a fixed density threshold, chosen to be 0.1, and the points locate the density maxima. For each plot, the vegetation types are ordered overall with increasing vegetation height, where lichen is the type with the smallest height and tree the type with the largest height. The gray lines on each plot delineate the achievable $H/\bar{\alpha}$ values.

Overall, taller vegetation classes show higher H and $\bar{\alpha}$ values than shorter vegetation classes. The vegetation diversity is most present at L-band, where all contour plots are more separated than at X- and C-band. At higher frequencies (C- and X-band) the variability among vegetation types is higher in winter compared to summer. This can be interpreted in the following way: in summer, the relatively dense vegetation saturates H and $\bar{\alpha}$ to, respectively, high and medium values that are characteristic of volume scattering. The SAR signal is only sensitive to the upper part of the canopy, and therefore vegetation types are not distinguishable. In winter, the vegetation is partially frozen and therefore more transparent, and the SAR signal is sensitive to the whole plant up to the ground. This could explain why different vegetation types can be better separated in winter. It has to be noted that at the frequency bands operated by the F-SAR sensor, the absorption and scattering in dry snow are generally considered negligible compared to the contribution from the ground below it [60]. In the event of above zero temperatures, the presence of ice inclusions in the snow could have an influence on the scattering, depending on the relative size of the snow grains and the radar wavelength. This would translate into an increase of the entropy and mean alpha angle, and this effect, though possibly present, would not explain the overall decreasing trend we observed [52]. Propagation effects in the snow could have a small influence on $H/\bar{\alpha}$ values. Indeed, as detailed in Section III-A2, the differential wave propagation at H and V polarizations through a snow layer with anisotropic structure can lead to different phase terms at HH and VV. This can lead to a change in the effective scattering matrix as measured by the SAR sensor, making it differ from the scattering matrix below the snow. This can in turn change the eigenvectors of the coherency matrix and therefore have an influence on the $\bar{\alpha}$, as explained in [59].

2) Copolar Phase Differences: CPD plots over the ROI are shown on Fig. 7. In summer, the CPD at L-band shows features along the streams where dense riparian shrubs grow and on the tree patch. This can be explained by the double-bounce occurring at the ground-trunk interfaces on these zones. C-band and X-band however exhibit much weaker CPD in summer. In winter, the trend is opposite, and X-band in particular shows recognizable CPD features. Topography or vegetation double-bounce effects can be excluded as this would also be visible in the summer map. Some linear features with large CPD (both positive and negative) can be associated with streams and backslopes where the snow accumulates, as can be seen on the snow depth reference map (see Fig. 2). As detailed in Section III-A, CPD can be caused by the propagation through an anisotropic media inducing a differential propagation for different polarization. In particular, a volume of nonspherical particles, such as fresh snow or firn, can be modeled as oblate and prolate spheroids and are expected to lead to negative and positive CPD (in our convention) [53]. The observed CPD on the ROI could be caused by this effect.

3) Change Analysis: We performed the polarimetric change analysis in two separate frames. On the one hand, we retrieved the seasonal change by applying the change analysis to the coherency matrices of winter and summer. On the other hand, we compared the vegetation types between each other by applying the change analysis to the mean of the coherency matrix, at fixed band and season, averaged over all the pixels of a given vegetation type.

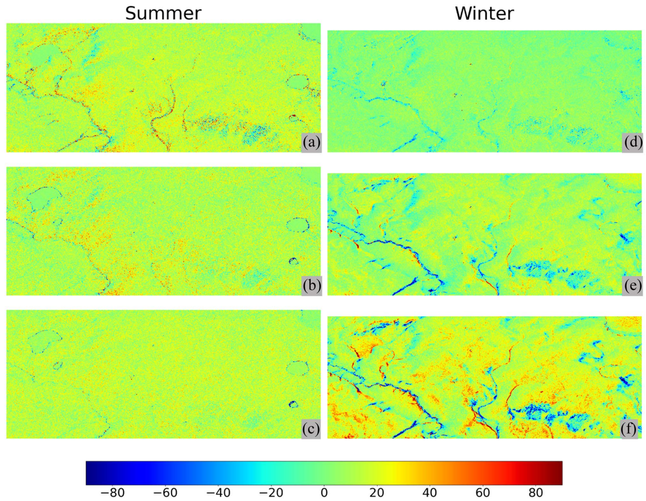

Fig. 7. CPD (in degrees). The left column contains the summer acquisitions at (a) L-band, (b) C-band, and (c) X-band. The right column contains the winter acquisitions at (d) L-band, (e) C-band, and (f) X-band.

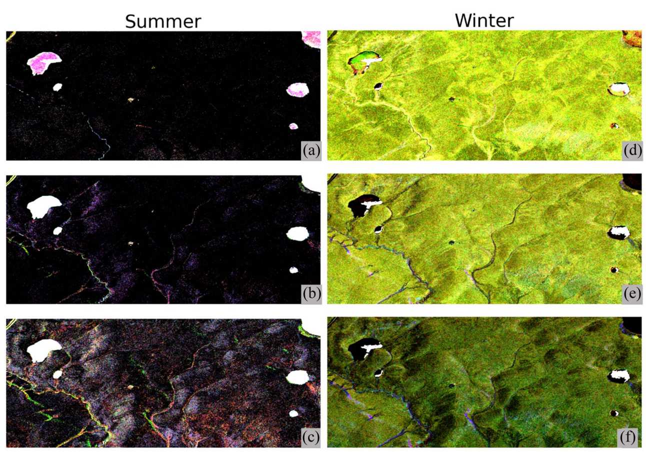

Fig. 8. Polarimetric change analysis: seasonal changes. The left column represents $p_{\text{inc}}^{\text{seasonal}}$ (scaling from 1 to 3 dB) the right column represents $p_{\text{dec}}^{\text{seasonal}}$ (scaling from 1 to 10 dB). The RGB colors correspond to the Pauli basis: red corresponds to the HH-VV channel, green to VH+HV and blue to HH+VV. White zones are invalid or saturated pixels. (a) and (d) Top, (b) and (e) middle, and (c) and (f) bottom rows contain L-, C-, and X-band results, respectively.

1) Seasonal change: The seasonal change analysis is applied, for each band separately, to the coherency matrix of winter and the coherency matrix of summer at each pixel. The change analysis results in three p_{inc} maps, denoted by $p_{\text{inc}}^{\text{seasonal}}$, and three p_{dec} maps, denoted by $p_{\text{dec}}^{\text{seasonal}}$; these six maps are shown on Fig. 8. The dark $p_{\text{inc}}^{\text{seasonal}}$ and bright $p_{\text{dec}}^{\text{seasonal}}$ indicate that all bands show a decrease from summer to winter in backscattering power of several dBs. Comparing bands, L-band shows the strongest decrease, while X-band shows the weakest. The predominant green color of all three p_{dec} maps indicate that the change occurs mostly at HV+VH, i.e., cross-polarization. This can be related to the decrease of the scattering due to the vegetation when it freezes, as could already be observed from $H/\bar{\alpha}$ in IV-A1. Features that can be attributed to vegetation types can be recognized. For instance, the brightest zones in the L-band $p_{\text{dec}}^{\text{seasonal}}$ encompass tall shrubs, riparian shrubs and tree areas, which are the zones with the tallest vegetation. This suggests that at L-band, taller vegetation types experience the largest decrease in volume and double-bounce scattering, which indicates that these vegetation stands become more transparent to the radar wave. On the contrary, some features corresponding to streams and riparian vegetation appear as darker patches within the X-band and C-band $p_{\text{dec}}^{\text{seasonal}}$ maps, suggesting that the decrease in power for those zones is not as severe compared to other vegetation types.

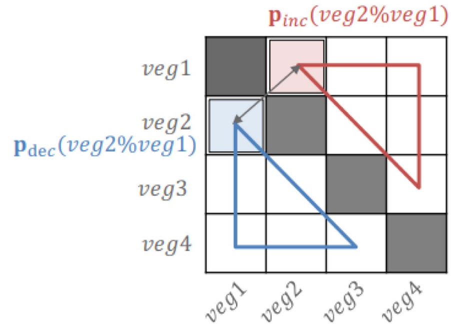

Fig. 9. The results of the polarimetric change analysis applied to different vegetation types can be organized into a matrix, where the upper diagonal contains the $p_{\text{inc}}^{\text{veg}}$ values and the lower diagonal the $p_{\text{dec}}^{\text{veg}}$ values, in the Pauli RGB basis.

2) Change between different vegetation types: The vegetation types are compared with respect to each other, at fixed season and band. Because the algorithm is applied to the mean coherency matrix over all pixels of each vegetation classes, the spatial information is aggregated into a single value: from one vegetation type to another, there is a single p_{inc} and and a single p_{dec} value, respectively denoted by $p_{\text{inc}}^{\text{veg}}$ and $p_{\text{dec}}^{\text{veg}}$. These values can be organized into matrices, as depicted on Fig. 9. The resulting matrices for each combination of band and season are shown on Fig. 10. For all arrays, brighter pixels at the top right corner indicate that vegetation types with larger heights (riparian shrub, trees) have overall a larger backscattering power compared to smaller vegetation types. These changes mostly take place in the VH+HV (green) and HH-VV (red) bands. These observations are consistent with the expected scenario where an increase of volume and double-bounce scattering components are obtained for increasing vegetation height. Patterns are similar for all arrays, with higher intensities at L-band compared to C- and X-band. It is interesting to note that, at X- and C-band, the contrast between short and large vegetation types is stronger in winter than in summer. This is consistent with the observation over H and $\bar{\alpha}$ in IV-A1: at higher frequencies, there is a saturation and the vegetation type is not a discriminating factor. In winter however, polarimetric indicators show a higher sensitivity to the vegetation type which can be due to the increased penetration into the frozen ground and the frozen canopy.

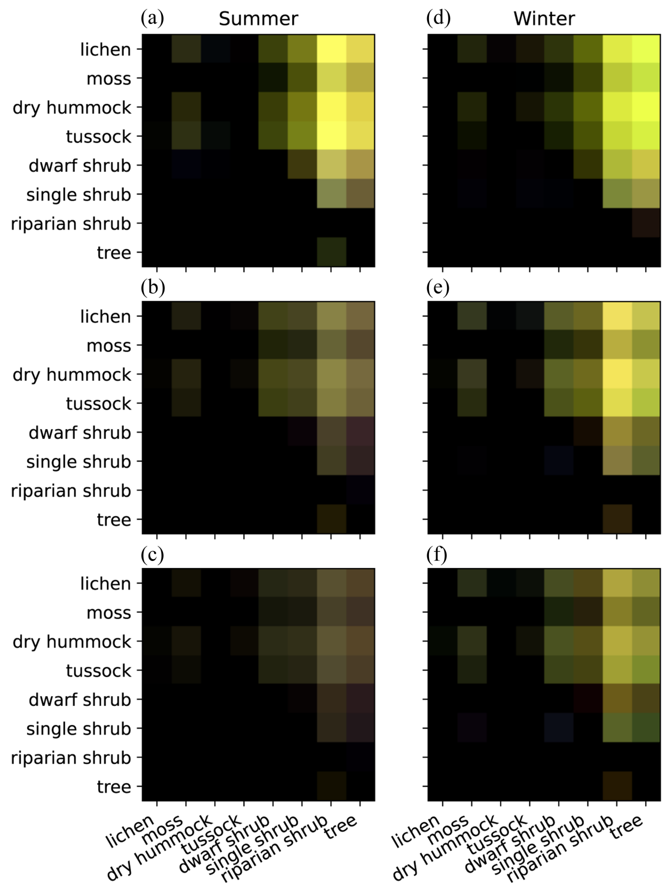

Fig. 10. Polarimetric change analysis: change between different vegetation types. The left column contains the summer results, the right column the winter results. (a) and (d) Top, (b) and (e) middle, and (c) and (f) bottom rows contain L-, C-, and X-band results, respectively. The vegetation types are overall ordered by height. The scale ranges from 0 to 10 dB, in the Pauli RGB basis.

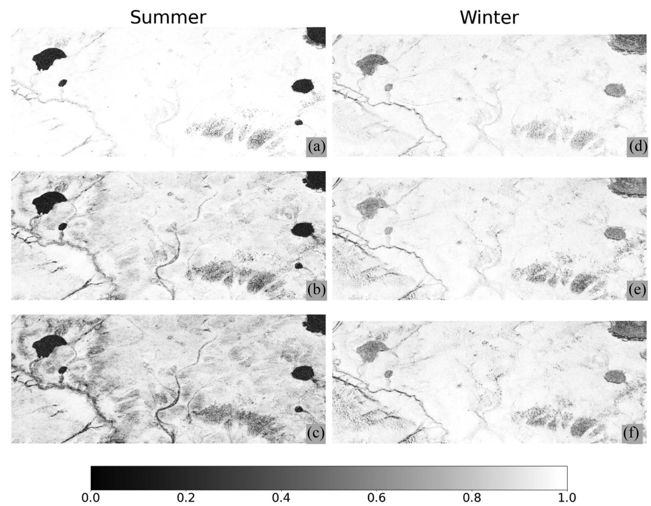

Fig. 11. Corrected coherence γ_{corr} over the ROI at HH polarization. The left column contains γ_{corr} computed from the summer acquisitions at (a) L-band, (b) C-band, and (c) X-band. The right column contains the winter acquisitions at (d) L-band, (e) C-band, and (f) X-band.

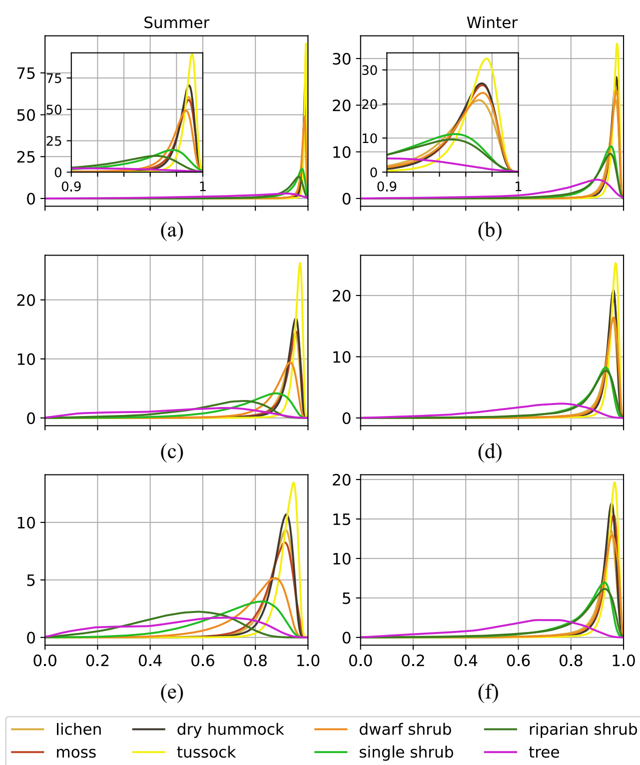

Fig. 12. Histograms of corrected coherence γ_{corr} over the ROI at HH polarization for different vegetation types. For L-band, an inset shows a zoom around the main peaks.

B. SAR Interferometry

Interferometry allows to add sensitivity to the vertical distribution of scatterers. The vertical sensitivity of an interferometric pair is driven by the vertical wavenumber defined in (5). Due to the dependency of k_z on λ, identical spatial baselines result into different vertical wavenumbers at different frequencies, therefore in order to have similar vertical sensitivity k_z for all frequencies, we selected different baselines for X-, C-, and L-band. More specifically, we selected the pairs of SLCs so that the vertical wavenumbers at X-, C-, and L-bands and for both seasons are close; over the ROI it averages to $k_z \approx 1$ rad/m.

1) Interferometric Coherence: As detailed in Section III-B, we performed various corrections in order to retrieve γ_{corr}. Assuming that $\gamma_{\text{temp}} = 1$, then γ_{corr} is close to the volume decorrelation, which is a function of the vertical reflectivity profile at each pixel. The maps of γ_{corr} over the ROI are shown in Fig. 11 and the corresponding histograms for different vegetation types are shown in Fig. 12. As all vertical wavenumbers are similar for all bands and seasons, the volume decorrelation depends solely on the vertical reflectivity profile, which is expected to vary with the season and the wavelength.

1) Effect of the wavelength: In summer, the corrected coherence varies greatly with the wavelength: shorter wavelengths present lower γ_{corr}. This is expected as at wavelength close to the size of vegetation elements, the wave is more likely to be scattered, making the vertical profile

more extended in height. In winter however, γ_{corr} is very similar for all wavelengths.

2) Effect of the season: At X- and C-band, the corrected coherence is lower in summer than in winter. This suggests that the above-ground scatterers have been at least partially removed, i.e., that the vegetation is more transparent to X- and C-band waves in winter. At L-band however, the corrected coherence is slightly lower in winter than in summer. This is consistent with the hypothesis that the L-band wave penetrates into the frozen ground in winter.

3) Effect of the vegetation type: In all bands and seasons, some particular patches that exhibit clearly strong decorrelation can be related to known high or dense vegetation, such as tree patches or the riparian shrub around the river channels. This can be seen from both the map and the histograms. Further on, there is for all bands and seasons a scaling of the corrected coherence with the vegetation height: taller vegetation types present smaller corrected coherence, while shorter vegetation types have a γ_{corr} closer to 1. There are only reduced differences inbetween short vegetation classes (lichen, moss, dry hummock, tussock). It can be noted that in summer at X- and C-band, pixels classified as dwarf shrubs present a γ_{corr} between the short vegetation and the tall vegetation types, while in winter these pixels have similar γ_{corr} than the short vegetation types. This suggests that the dwarf shrubs of the ROI become transparent to X- and C-band waves in winter conditions.

2) Interferometric Phase: The interferometric phases at L-band were calibrated with a corner reflector as explained in III-B2 and transferred to phase center heights by means of the vertical wavenumber k_z. Only a limited region around the corner reflector was considered calibrated, as the expected phase screens are assumed to change smoothly in space. After calibration, the phase center height may be related to the vegetation height. The phase center heights are shown on Fig. 13. It is to be noted that, even if there is penetration into the frozen soil, no correction is performed on the wavenumber to account for this possible propagation, therefore the retrieved maps are related to but not equal to penetration depths. The observed negative phases (and heights) can be explained by the fact that at L-band, the phase center height in summer is close to the ground for short and mid vegetation, while it can be biased upward in the ALS that is used as a reference if the vegetation is very dense. Overall, phase center heights are deeper in winter than summer.

Four patches with homogeneous vegetation type were selected as shown on Fig. 14. We considered two homogeneous patches of dwarf shrubs, referred to as S1 and S2, as well as two homogeneous patches of dry hummock, referred to as H1 and H2. The boxplot of their phase center height in summer and winter is shown on Fig. 15. It can be observed that both dwarf shrub sites exhibit similar values of phase center heights in winter and summer. The two dry hummock sites have slightly different phase center heights at both seasons, but the difference between both seasons is very similar. Overall, the four sites show a significant decrease of several tens of centimeters of their phase

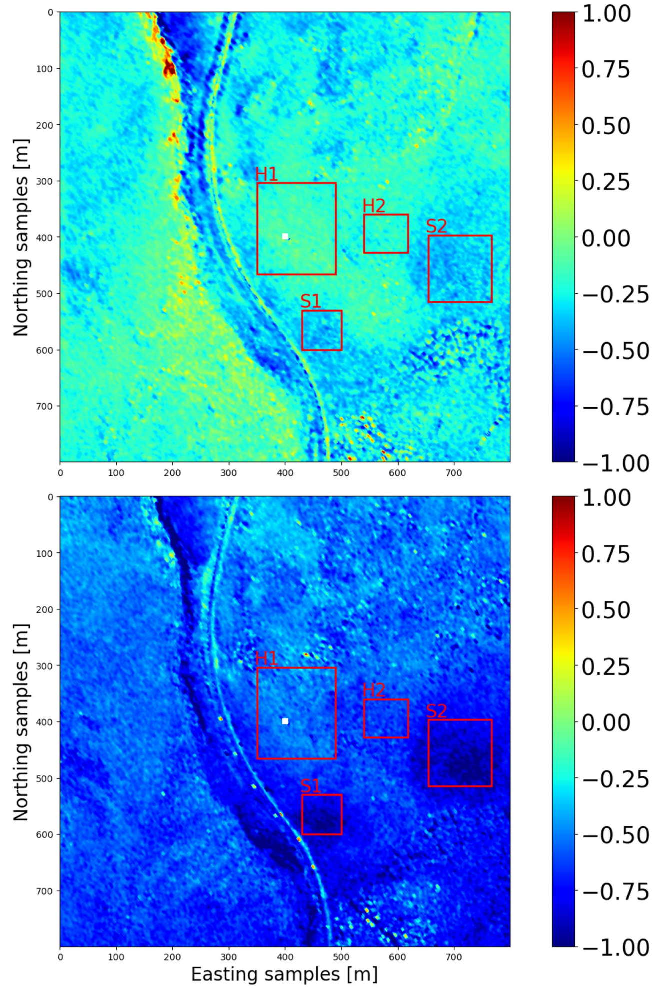

Fig. 13. Top plot: Height from calibrated phase in summer, at L-band, VV polarization. Bottom plot: Height from calibrated phase in winter, at L-band, VV polarization. The phase at HH+VV at the corner reflector is taken as reference. The corner reflector is at the center of the images, it has been masked out and appears white. The linear structure in the middle of each plot is the Inuvik–Tuktoyaktuk Highway. Both grids are in geographic coordinates. Both scales are in meters.

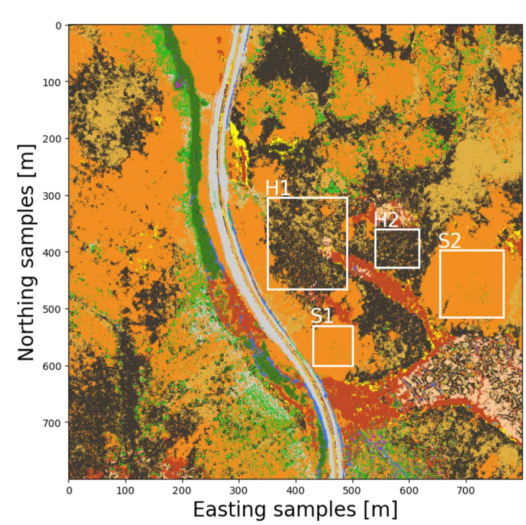

Fig. 14. Vegetation map at the vicinity of the corner reflector. The legend is the same as on Fig. 2.

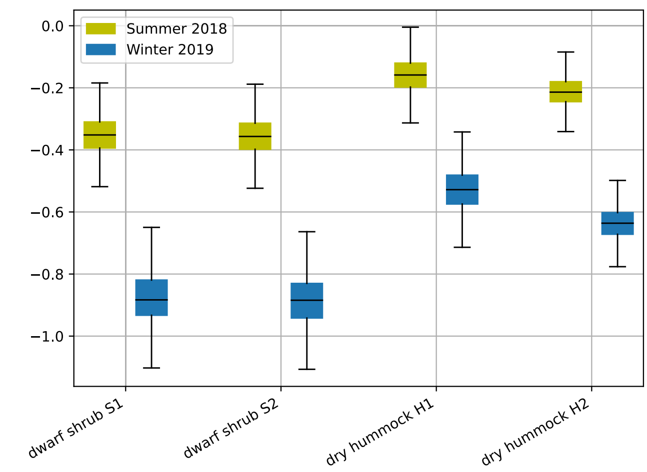

Fig. 15. Boxplot of calibrated phase center height (in meters) at L-band, computed with the vertical wavenumber in air, over four homogeneous patches defined on Fig. 13.

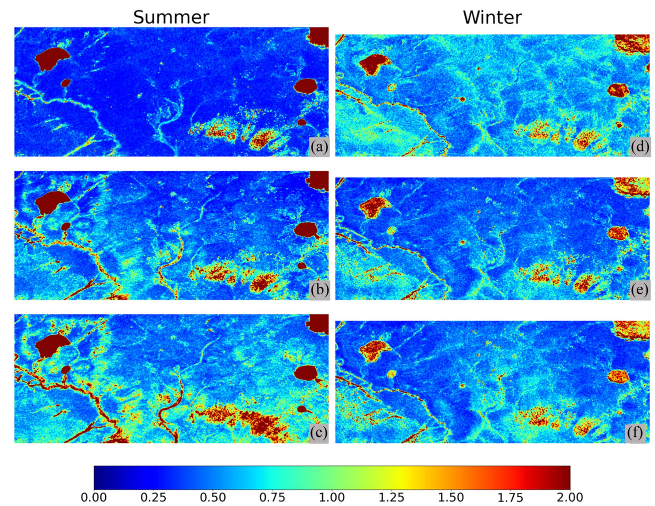

Fig. 16. Pol-InSAR coherence region height extent Δh (in meters). Maximum filtering over 5 m $\times$ 5 m patches has been performed in order to enhance the features. The left column contains Δh computed from the summer acquisitions at (a) L-band, (b) C-band, and (c) X-band. The right column contains Δh computed from the winter acquisitions at (d) L-band, (e) C-band, and (f) X-band.

center height from summer to winter. This is probably related to the penetration into the frozen soil in winter.

3) Penetration Into the Frozen Ground: In order to confirm the observations consistent with penetration into the frozen ground in winter, we can compute the power penetration depth of the radar wave into the soil. For this, it is crucial to know the complex dielectric constant of the frozen ground on our site, either from experiments on similar soils or from a model. Several studies have performed such microwave dielectric measurements [10], [61] and several models have been developed [62], [63], [64]. When the soil water is frozen, the soil dielectric constant varies only weakly with the radar frequency, and is more subject to dependency on the soil temperature [65] and soil composition [61]. On TVC, the AWI teams have installed a temperature and volumetric soil moisture profile, which permanently records ground temperature every hour at 2, 5, 10, and 20 cm depth [66]. In March 2019, the recorded ground temperatures varied between -10°C and -4.5°C. On the 23rd of March 2019, which is the F-SAR flight date, the ground temperature was recorded to vary between -7.8°C and -6.8°C, all depths considered. Regarding the soil composition, Quinton and Pomeroy [38] report that in the upper 30 cm of the soil, the proportion of sand, silt, and clay are roughly the same in the mineral hummocks, while the inter hummock zone is composed of a thick peat layer. This means that the soil type varies at meter scale in hummock zones, and it also varies within the ROI in correlation with the vegetation type. Due to the pixel size after multilooking (approximately 5 m $\times$5 m in the slant range-azimuth coordinates), it is very likely that a single SAR pixel encompasses several soil types. As a consequence, we avoid assumptions on the soil type and consider real and imaginary permittivities to be $\epsilon'_{\text{frozen}} = 5$ and $\epsilon''_{\text{frozen}} = 0.5$, respectively, in the frozen soil case to give a good first approximation [61].

Then, we can derive the power-penetration depth, defined in [67] as the depth at which the power of the electromagnetic wave propagating in a homogeneous medium is reduced by a factor of e. As $\epsilon''_{\text{frozen}} << \epsilon'_{\text{frozen}}$, the penetration depth is approximated as

$$\delta = \frac{\lambda\sqrt{\epsilon'_{\text{frozen}}}}{2\pi\epsilon''_{\text{frozen}}} \tag{7}$$

where λ is the SAR wavelength. At L-band, we find $\delta = 16$ cm as an order of magnitude, and the observed difference in phase center height between winter and summer is slightly higher in the order of tens of cm. This confirms that the phase center height obtained in winter at L-band, which is several tens of centimeters below the phase center of summer, is compatible with penetration of the electromagnetic wave in the frozen ground at this frequency.

C. Polarimetric SAR Interferometry

The maps of the Pol-InSAR coherence region extent in phase and norm are shown on Figs. 16 and 17, respectively. The associated boxplots for each vegetation type are represented on Figs. 18 and 19.

1) Effect of the Wavelength: In summer, both the maps and the boxplots indicate larger Δh and $\Delta|\gamma|$ for smaller wavelengths compared to larger wavelengths, for all vegetation types. This can be due to either the variance of phases associated with smaller coherence at smaller wavelengths, or to a more extended and polarization-dependent vertical reflectivity profile over vegetation patches at smaller wavelengths. In winter, this effect is not present. From the maps, it can be observed that L-band shows larger Δh and $\Delta|\gamma|$ compared to X- and C-band, for which the values are close to each other. From the boxplots, it appears that this increase is mostly occurring for short vegetation types, while taller vegetation types have similar Δh and $\Delta|\gamma|$ across wavelengths.

2) Effect of the Season: At L-band, the difference between summer and winter is large, both for Δh and $\Delta|\gamma|$. Δh shows

TABLE III
SUMMARY OF THE RESULTS—OBSERVATIONS

<table>
<tr><th></th><th></th><th>X-band</th><th>C-band</th><th>L-band</th></tr>
<tr><td rowspan="5">PolSAR</td><td>Entropy/alpha</td><td>• decrease of H and $\bar{\alpha}$ from summer to winter
• summer: no vegetation diversity
• winter: weak vegetation diversity</td><td>• decrease of H and $\bar{\alpha}$ from summer to winter
• summer and winter: weak vegetation diversity</td><td>• decrease of H and $\bar{\alpha}$ from summer to winter
• summer and winter: strong vegetation diversity</td></tr>
<tr><td>CPD</td><td>• summer: weak
• winter: strong, at sites with large snow depth</td><td>• summer: weak
• winter: present</td><td>• summer: strong at riparian shrubs and trees sites
• winter: weak</td></tr>
<tr><td>Change analysis:</td><td></td><td></td><td></td></tr>
<tr><td>Seasonal change</td><td>• weak decrease from summer to winter
• decrease at VH+HV
• some linear features related to the snow</td><td>• decrease from summer to winter
• decrease at VH+HV and HH-VV</td><td>• strong decrease from summer to winter
• strongest change for tall vegetation
• decrease at VH+HV and HH-VV</td></tr>
<tr><td>Change between different vegetation types</td><td>• increase from short to tall vegetation types
• polarisation: VH+HV and HH-VV
• stronger increase in winter</td><td>• increase from short to tall vegetation types
• polarisation: VH+HV and HH-VV
• stronger increase in winter</td><td>• increase from short to tall vegetation types
• polarisation: VH+HV and HH-VV
• summer and winter: similar</td></tr>
<tr><td rowspan="2">InSAR</td><td>Interferometric coherence</td><td>• increases from summer to winter</td><td>• increases from summer to winter</td><td>• decreases from summer to winter</td></tr>
<tr><td>Interferometric phase</td><td>/</td><td>/</td><td>• decrease of the phase center height from summer to winter
• winter phase center height is < 0</td></tr>
<tr><td>Pol-InSAR</td><td>Coherence region shape</td><td>• summer: the shape is related to the vegetation type</td><td>• summer: the shape is related to the vegetation type</td><td>• summer: the shape is related to the vegetation type
• winter: short vegetation types have larger Δh and $\Delta\lvert\gamma\rvert$</td></tr>
</table>

TABLE IV
SUMMARY OF THE RESULTS - INTERPRETATION

<table>
<tr><th></th><th></th><th>X-band</th><th>C-band</th><th>L-band</th></tr>
<tr><td rowspan="5">PolSAR</td><td>Entropy/alpha</td><td>• summer: saturation due to important volume scattering from vegetation
• winter: desaturation, more sensitivity to the vegetation type</td><td>• summer: saturation due to important volume scattering from vegetation
• winter: desaturation, more sensitivity to the vegetation type</td><td>• winter: trend towards more surface scattering than summer</td></tr>
<tr><td>CPD</td><td>• winter: related to deep snow patterns</td><td>• winter: related to deep snow patterns</td><td>• summer: related to the double bounce of vegetation</td></tr>
<tr><td>Change analysis:</td><td></td><td></td><td></td></tr>
<tr><td>Seasonal change</td><td>• the vegetation becomes more transparent in winter due to freezing</td><td>• the vegetation becomes more transparent in winter due to freezing</td><td>• the vegetation becomes more transparent in winter due to freezing • effect of vegetation freezing most clear for tall vegetation types</td></tr>
<tr><td>Change between different vegetation types</td><td>• summer: saturation due to important volume scattering from vegetation
• winter: desaturation, more sensitivity to the vegetation type</td><td>• summer: saturation due to important volume scattering from vegetation
• winter: desaturation, more sensitivity to the vegetation type</td><td>• relative changes between vegetation types do not vary with season</td></tr>
<tr><td rowspan="2">InSAR</td><td>Interferometric coherence</td><td>• vegetation more transparent</td><td>• vegetation more transparent</td><td>• suggests penetration into the frozen ground</td></tr>
<tr><td>Interferometric phase</td><td>/</td><td>/</td><td>• suggests penetration into the frozen ground</td></tr>
<tr><td>Pol-InSAR</td><td>Coherence region shape</td><td>• depends on the vegetation in summer but not in winter</td><td>• depends on the vegetation in summer but not in winter</td><td>• consistent with penetration into the frozen ground in winter</td></tr>
</table>

an increase from summer to winter on regions with short vegetation types, while larger vegetation types see less apparent changes. This can be observed both on the maps and on the boxplots.

At C-band, from the map, it seems that the dynamic range of Δh is conserved from summer to winter but with a different spatial distribution. This is consistent with the observation that the boxplots do not vary significantly with the season, except for zones of riparian shrubs, where Δh decreases from summer to winter. These observations are similar for $\Delta|\gamma|$. This suggests that the phase center heights spread is not related with the vegetation type but to other effects, for instance decorrelation linked to snow patterns.

At X-band, the behavior is similar to C-band. There is a clear decrease of Δh at streams with riparian shrubs and at the forest zone. This can be related to the transparency of the frozen vegetation, as X- and C-band waves are less likely to reach the ground in the case of taller vegetation and therefore to be influenced by the frozen/thawed state of the ground. For the short vegetation types, Δh decreases in some regions and increase in other regions. The boxplots also do not vary very notably for short vegetation types.

3) Effect of the Vegetation Type: At L-band in summer, Δh as well as $\Delta|\gamma|$ are larger at regions with taller vegetation types. This appears clearly in the boxplots, with a scaling from shorter vegetation types (on the left of Figs. 18 and 19) to taller

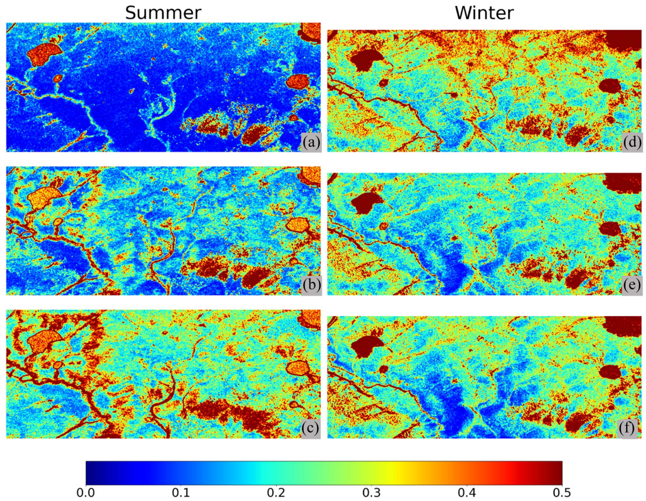

Fig. 17. Pol-InSAR coherence region norm extent $\Delta|\gamma|$. Maximum filtering over 5 m $\times$ 5 m patches has been performed in order to enhance the features. The left column contains $\Delta|\gamma|$ computed from the summer acquisitions at at (a) L-band, (b) C-band, and (c) X-band. The right column contains $\Delta|\gamma|$ computed from the winter acquisitions at (d) L-band, (e) C-band, and (f) X-band.

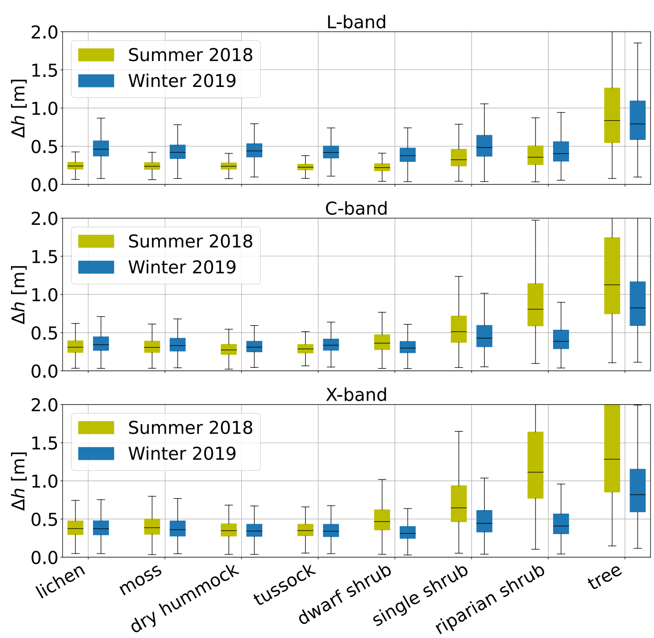

Fig. 18. Boxplots of Δh in summer and winter, at L-, C-, and X-band, separated according to the vegetation type. The vegetation types have been ordered by height, where shorter vegetation types are located on the left of the x-axis, and larger vegetation types on the right.

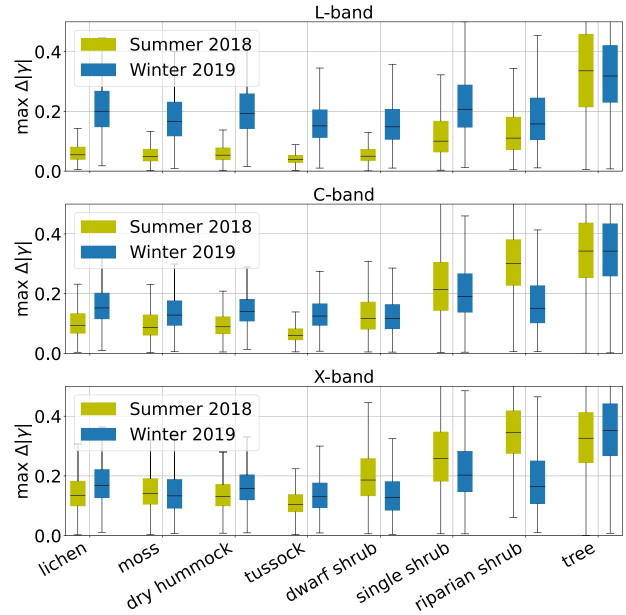

Fig. 19. Boxplot of $\Delta|\gamma|$ in summer and winter, at L-, C-, and X-band, separated according to the vegetation type. The vegetation types are ordered similarly to Fig. 18.

vegetation types (on the right of the same boxplots). At L-band in winter, this effect is less clear. Only regions covered by trees still appear with a larger Δh and $\Delta|\gamma|$, and overall the values of Δh and $\Delta|\gamma|$ are similar for the other shorter vegetation types, translating into a flattening of the boxplots.

At C-band in summer, Δh and $\Delta|\gamma|$ are larger for taller vegetation types. The boxplots, like in summer, show a clear increase of Δh and $\Delta|\gamma|$ for increasing vegetation heights. Contrary to L-band however, the dwarf shrub pixels exhibit larger values compared to smaller vegetation types. At C-band in winter, taller vegetation types appear clearly with higher Δh and $\Delta|\gamma|$, however the other regions with large values do not seem to be correlated with a certain vegetation type. This is consistent with the boxplots being very flat across the vegetation types.

At X-band in summer, the trend is similar to C-band in summer, with, in the case of Δh, even larger discrepancies between shorter and larger vegetation types. At X-band in winter, the trends are similar to C-band in winter.

V. Conclusion

In this study, we have retrieved various polarimetric, interferometric and polarimetric–interferometric SAR observables over a test site located in the Canadian low Arctic permafrost region. We analyzed the variability of the products across several dimensions, including the three frequencies (X-band, C-band, and L-band), and both summer and winter seasons. As the considered test site is covered by different vegetation types, we could take into account the vegetation diversity. It is important to note that the airborne SAR dataset consists in flights with nonzero spatial baselines, and short temporal baselines, therefore the interferometric complex coherence computed in this article reflects the volume decorrelation due to the vertical distribution of scatterers within each pixel.

The results of the data analysis are summarized in Tables III and IV according to method and radar band. Table III summarizes the main observations, for each method and radar band, while Table IV presents the physical interpretation of these observations. These interpretations relate the observables to the elements that the SAR signal is sensitive to in the scene: the snow in winter, the vegetation characteristics for both seasons, and the frozen ground in winter.

1) Regarding the snow characteristics, it could be observed that on the test site the X-band polarimetric signal is more sensitive to the presence of snow patches. This was mostly to be seen in the winter CPD at X-band, which was related to snow depth patterns.
2) Regarding the vegetation characteristics, the observations suggest that the vegetation is partially frozen in winter, leading to a decrease in the dielectric constant and making it more transparent to the radar waves of all bands. This was derived from several observations. The first indication was the overall decrease in polarimetric entropy and mean alpha angle, at all bands, from summer to winter. The second indication was the decrease in scattering power from summer to winter at all bands, occurring mostly at HV+VH polarization, which is in natural scenes mostly associated to scattering from the vegetation. Finally, the increase in coherence at X- and C-band from summer to winter, for a similar vertical wavenumber, suggests less volume decorrelation in the scene in winter and is consistent with the presence of a vegetation volume that is transparent to scattering. It should be noted that these observations indicate qualitatively that the vegetation is *more* transparent in winter than summer, but they do not provide an assessment of whether the vegetation is completely frozen or not.
3) We could also observe that the sensitivity of the retrieved indicators to vegetation type was different for different bands and seasons. This was indicated by the saturation of the polarimetric entropy and the mean alpha angle in summer, while these parameters were sensitive to the vegetation types in winter. This was confirmed by the polarimetric change analysis, where we could observe that the differences between vegetation types, at X- and C-band, were small in summer while larger differences could be observed in winter.
4) Finally, the winter observables were consistent with penetration into the frozen ground at L-band, which to the best of the authors knowledge has never been observed before. This was indicated by the interferometric observables. More specifically, the smaller coherence in winter compared to summer, and a deeper phase center height in winter compared to summer, were consistent with volume decorrelation occurring below the surface. This was also indicated by the increase in the Pol-InSAR coherence region shape parameters Δh and $\Delta|\gamma|$ in winter compared to summer.

This study and its conclusions are relevant in particular for future satellite SAR missions operating at L-band. Upcoming L-band systems include ESA's Radar Observing System for Europe at L-Band (ROSE-L) and NASA-ISRO SAR Mission (NISAR). Both missions plan a global coverage and list permafrost characteristics as secondary and primary science objectives respectively [68], [69]. DInSAR time series that include winter acquisitions will have to account for the penetration of the signal into the frozen ground, as this might bias the estimated deformation. Furthermore, an extension of ROSE-L to single-pass could provide more insights into ground properties of frozen landscapes. At all frequency bands, the use of fully polarimetric data is promising to analyze the vegetation and soil characteristics, also from a seasonal perspective. This is the case for ROSE-L and NISAR as both missions will have dual and quad-pol capabilities, and also for current missions with such polarimetric capabilities (ALOS-2, Radarsat-2, TerraSAR-X, Sentinel-1 ...). Multifrequency approaches including X-, C-, and L-band, from for instance TanDEM-X, Sentinel-1, and ROSE-L would provide complete information by increasing the SAR observation space.

As a result of the study it can be noted that winter SAR acquisitions over lowland permafrost areas are of high interest and need to be better understood. Further studies could focus not only on the freeze-thaw transition in time series, but also on the winter observables individually. Potential winter variables of interest include the residual water content in tundra vegetation and the residual water content in the frozen soil.

Acknowledgment

The authors would like to thank the DLR F-SAR processing team for the acquisition and pre-processing of the PermASAR dataset, in particular Marc Jäger.

References

[1] S. Westermann, C. R. Duguay, G. Grosse, and A. Kääb, "Remote sensing of permafrost and frozen ground," in *Remote Sensing of the Cryosphere*. New York, NY, USA: Wiley, 2014, pp. 307–344.
[2] A. Bartsch, T. Strozzi, and I. Nitze, "Permafrost monitoring from space," *Surv. Geophys.*, vol. 44, no. 5, pp. 1579–1613, Mar. 2023.
[3] "Intergovernmental panel on climate change (IPCC)," in *Climate Change 2021–The Physical Science Basis: Working Group I Contribution to the Sixth Assessment Report of the Intergovernmental Panel on Climate Change*. Cambridge, U.K.: Cambridge Univ. Press, 2023.
[4] G. Grosse et al., "Vulnerability of high-latitude soil organic carbon in North America to disturbance," *J. Geophysical Res.*, vol. 116, Jul. 2011, Art. no. G00K06.
[5] E. A. G. Schuur et al., "Climate change and the permafrost carbon feedback," *Nature*, vol. 520, no. 7546, pp. 171–179, Apr. 2015.
[6] H. M. French, *The Periglacial Environment*. Hoboken, NJ, USA: Wiley, 2007.
[7] U. Wegmüller, "The effect of freezing and thawing on the microwave signatures of bare soil," *Remote Sens. Environ.*, vol. 33, no. 2, pp. 123–135, Aug. 1990.
[8] E. Rignot and J. B. Way, "Monitoring "freezethaw" cycles along "North-South" Alaskan transects using ERS-1 SAR," *Remote Sens. Environ.*, vol. 49, no. 2, pp. 131–137, Aug. 1994.
[9] L. Liu, T. Zhang, and J. Wahr, "InSAR measurements of surface deformation over permafrost on the North Slope of Alaska," *J. Geophysical Res.*, vol. 115, Aug. 2010, Art. no. F03023, doi: 10.1029/2009JF001547.
[10] M. T. Hallikainen, F. T. Ulaby, M. C. Dobson, M. A. El-Rayes, and L.-K. Wu, "Microwave dielectric behavior of wet soil-part 1: Empirical models and experimental observations," *IEEE Trans. Geosci. Remote Sens.*, vol. GE-23, no. 1, pp. 25–34, Jan. 1985.
[11] R. Bamler and P. Hartl, "Synthetic aperture radar interferometry," *Inverse Problems*, vol. 14, no. 4, pp. R1–R54, Aug. 1998.
[12] S. Cloude and E. Pottier, "An entropy based classification scheme for land applications of polarimetric SAR," *IEEE Trans. Geosci. Remote Sens.*, vol. 35, no. 1, pp. 68–78, Jan. 1997.
[13] S.-E. Park, A. Bartsch, D. Sabel, W. Wagner, V. Naeimi, and Y. Yamaguchi, "Monitoring freeze/thaw cycles using ENVISAT ASAR global mode," *Remote Sens. Environ.*, vol. 115, no. 12, pp. 3457–3467, Dec. 2011.
[14] J. Du, J. S. Kimball, M. Azarderakhsh, R. S. Dunbar, M. Moghaddam, and K. C. McDonald, "Classification of Alaska spring thaw characteristics using satellite L-band radar remote sensing," *IEEE Trans. Geosci. Remote Sens.*, vol. 53, no. 1, pp. 542–556, Jan. 2015.

[15] R. H. Chen, A. Tabatabaeenejad, and M. Moghaddam, "Retrieval of permafrost active layer properties using time-series P-band radar observations," *IEEE Trans. Geosci. Remote Sens.*, vol. 57, no. 8, pp. 6037–6054, Aug. 2019.

[16] T. Jagdhuber, J. Stockamp, I. Hajnsek, and R. Ludwig, "Identification of soil freezing and thawing states using SAR polarimetry at C-band," *Remote Sens.*, vol. 6, no. 3, pp. 2008–2023, Mar. 2014.

[17] J. Khaldoune, E. van Bochove, M. Bernier, and M. C. Nolin, "An approach for mapping frozen soil of agricultural land under snow cover using RADARSAT-1 and RADARSAT-2," in *Proc. IEEE Int. Geosci. Remote Sens. Symp.*, 2008, pp. III-382–III-385.

[18] L.-P. Rousseau, R. Magagi, R. Leconte, A. Berg, and B. Toth, "Potentials of RADARSAT-2 data to monitor freezing/thawing cycles over agricultural lands in Canada," in *Proc. IEEE Int. Geosci. Remote Sens. Symp.*, 2009, pp. II–598–II–601.

[19] R. P. Rykhus and Z. Lu, "InSAR detects possible thaw settlement in the Alaskan arctic coastal plain," *Can. J. Remote Sens.*, vol. 34, no. 2, pp. 100–112, Jan. 2008.

[20] N. Short, B. Brisco, N. Couture, W. Pollard, K. Murnaghan, and P. Budkewitsch, "A comparison of TerraSAR-X, RADARSAT-2 and ALOS-PALSAR interferometry for monitoring permafrost environments, case study from Herschel Island, Canada," *Remote Sens. Environ.*, vol. 115, no. 12, pp. 3491–3506, Dec. 2011.

[21] L. Liu, K. Schaefer, T. Zhang, and J. Wahr, "Estimating 1992-2000average active layer thickness on the Alaskan North Slope from remotely sensed surface subsidence," *J. Geophysical Res.: Earth Surf.*, vol. 117, no. F1, Jan. 2012, Art. no. 1005.

[22] K. Schaefer et al., "Remotely sensed active layer thickness (ReSALT) at Barrow, Alaska using interferometric Synthetic Aperture Radar," *Remote Sens.*, vol. 7, no. 4, pp. 3735–3759, Mar. 2015.

[23] S. Zwieback and F. J. Meyer, "Top-of-permafrost ground ice indicated by remotely sensed late-season subsidence," *Cryosphere*, vol. 15, no. 4, pp. 2041–2055, Apr. 2021.

[24] S. Zwieback, G. Iwahana, S. Sakhalkar, R. Biessel, S. Taylor, and F. J. Meyer, "Excess ground ice profiles in continuous permafrost mapped from InSAR subsidence," *Water Resour. Res.*, vol. 60, no. 2, Feb. 2024, Art. no. e2023WR035331. [Online]. Available: https://doi.org/10.1029/2023WR035331

[25] S. Daout, B. Dini, W. Haeberli, M.-P. Doin, and B. Parsons, "ICE loss in the Northeastern Tibetan Plateau permafrost as seen by 16 yr of ESA SAR missions," *Earth Planet. Sci. Lett.*, vol. 545, Sep. 2020, Art. no. 116404.

[26] G. Iwahana et al., "InSAR detection and field evidence for thermokarst after a tundra wildfire, using ALOS-PALSAR," *Remote Sens.*, vol. 8, no. 3, Mar. 2016, Art. no. 218.

[27] S. Antonova et al., "Thaw Subsidence of a Yedoma Landscape in Northern Siberia, Measured In Situ and Estimated from TerraSAR-X Interferometry," *Remote Sens.*, vol. 10, no. 4, Mar. 2018, Art. no. 494.

[28] L. Rouyet, T. R. Lauknes, H. H. Christiansen, S. M. Strand, and Y. Larsen, "Seasonal dynamics of a permafrost landscape, Adventdalen, Svalbard, investigated by InSAR," *Remote Sens. Environ.*, vol. 231, Sep. 2019, Art. no. 111236.

[29] T. Strozzi et al., "Sentinel-1 SAR interferometry for surface deformation monitoring in low-land permafrost areas," *Remote Sens.*, vol. 10, no. 9, Aug. 2018, Art. no. 1360.

[30] T. Ullmann, S. N. Banks, A. Schmitt, and T. Jagdhuber, "Scattering characteristics of X-, C- and L-band PolSAR data examined for the tundra environment of the Tuktoyaktuk Peninsula Canada," *Appl. Sci.*, vol. 7, no. 6, Jun. 2017, Art. no. 595.

[31] S. Zwieback and A. A. Berg, "Fine-scale SAR soil moisture estimation in the Subarctic tundra," *IEEE Trans. Geosci. Remote Sens.*, vol. 57, no. 7, pp. 4898–4912, Jul. 2019.

[32] T. Ullmann et al., "Land cover characterization and classification of Arctic tundra environments by means of polarized Synthetic Aperture X- and C-band radar (PolSAR) and Landsat 8 multispectral imagery Richards Island, Canada," *Remote Sens.*, vol. 6, no. 9, pp. 8565–8593, Sep. 2014.

[33] Y. Huang et al., "Permafrost Dynamics Observatory (PDO): 2. Joint retrieval of permafrost active layer thickness and soil moisture from L-band InSAR and P-band PolSAR," *Earth Space Sci.*, vol. 10, 2023, Art. no. e2022EA002453. [Online]. Available: https://doi.org/10.1029/2022EA002453

[34] A. Judge, "Permafrost distribution and the Quaternary history of the Mackenzie-Beaufort region: A geothermal perspective," in *Proc. Correlation Quaternary Deposits Events Around Margin Beaufort Sea: Contributions Joint Can.- Amer. Workshop*, 1986, pp. 41–45.

[35] P. Marsh et al., *Snowmelt Processes and Runoff At the Arctic Treeline: Ten Years of MAGS Research*. Berlin, Germany: Springer, 2008, pp. 97–123.

[36] I. Grünberg, E. J. Wilcox, S. Zwieback, P. Marsh, and J. Boike, "Linking tundra vegetation, snow, soil temperature, and permafrost," *Biogeosciences*, vol. 17, no. 16, pp. 4261–4279, Aug. 2020.

[37] Environment and climate change Canada, canadian climate normals. (n.d.). [Online]. Available: http://climate.weather.gc.ca/climate_normals/

[38] W. L. Quinton and J. W. Pomeroy, "Transformations of runoff chemistry in the Arctictundra, Northwest Territories, Canada," *Hydrological Processes*, vol. 20, no. 14, pp. 2901–2919, Jun. 2006.

[39] P. Marsh, P. Bartlett, M. MacKay, S. Pohl, and T. Lantz, "Snowmelt energetics at a shrub tundra site in the Western Canadian Arctic," *Hydrological Processes*, vol. 24, no. 25, pp. 3603–3620, Nov. 2010.

[40] J. King et al., "The influence of snow microstructure on dual-frequency radar measurements in a tundra environment," *Remote Sens. Environ.*, vol. 215, pp. 242–254, Sep. 2018.

[41] N. Rutter et al., "Effect of snow microstructure variability on Ku-band radar snow water equivalent retrievals," *Cryosphere*, vol. 13, no. 11, pp. 3045–3059, Nov. 2019.

[42] C. Voigt et al., "Arctic soil methane sink increases with drier conditions and higher ecosystem respiration," *Nature Climate Change*, vol. 13, no. 10, pp. 1095–1104, Aug. 2023.

[43] S. Antonova et al., "Estimating tree height from TanDEM-X data at the northwestern Canadian treeline," *Remote Sens. Environ.*, vol. 231, Sep. 2019, Art. no. 111251.

[44] E. J. Wilcox et al., "Tundra shrub expansion may amplify permafrost thaw by advancing snowmelt timing," *Arctic Sci.*, vol. 5, no. 4, pp. 202–217, Dec. 2019.

[45] I. Hajnsek et al., "DLR airborne SAR campaign on permafrost soils and boreal forests in the Canadian Northwest Territories, Yukon and Saskatchewan: PermASAR," in *Proc. 9th Int. Workshop Sci. Appl. SAR Polarimetry Polarimetric Interferometry*, 2019.

[46] A. Reigber et al., "Very-high-resolution airborne Synthetic Aperture radar imaging: Signal processing and applications," *Proc. IEEE*, vol. 101, no. 3, pp. 759–783, Mar. 2013.

[47] V. R. Dutch et al., "Impact of measured and simulated tundra snowpack properties on heat transfer," *Cryosphere*, vol. 16, no. 10, pp. 4201–4222, Oct. 2022.

[48] S. Lange, I. Grünberg, K. Anders, J. Hartmann, V. Helm, and J. Boike, "Airborne Laser Scanning (ALS) point clouds of Trail Valley Creek, NWT, Canada (2018)," 2021. [Online]. Available: https://doi.org/10.1594/PANGAEA.934387

[49] I. Grünberg and J. Boike, "Vegetation map of Trail Valley Creek, Northwest Territories, Canada," 2019. [Online]. Available: https://doi.org/10.1594/PANGAEA.904270

[50] J. Hammar, I. Grünberg, S. Hendricks, A. Jutila, V. Helm, and J. Boike, "Snow covered digital elevation model and snow depth product (2019), Trail Valley Creek, NWT, Canada," 2023. [Online]. Available: https://doi.org/10.1594/PANGAEA.962552

[51] J. Hammar, I. Grünberg, S. V. Kokelj, J. van der Sluijs, and J. Boike, "Snow accumulation, albedo and melt patterns following road construction on permafrost, Inuvik–Tuktoyaktuk Highway, Canada," *Cryosphere*, vol. 17, no. 12, pp. 5357–5372, Dec. 2023.

[52] G. Parrella, I. Hajnsek, and K. Papathanassiou, "On the interpretation of L- and P-band PolSAR signatures of polythermal glaciers," in *Proc. ESA POLinSAR Workshop*, 2013, pp. 1–6.

[53] S. Leinss, G. Parrella, and I. Hajnsek, "Snow height determination by polarimetric phase differences in X-band SAR data," *IEEE J. Sel. Topics Appl. Earth Observ. Remote Sens.*, vol. 7, no. 9, pp. 3794–3810, Sep. 2014.

[54] A. A. González, C. López Martínez, K. Papathanassiou, and I. Hajnsek, "Polarimetric SAR time series change analysis over agricultural areas," *IEEE Trans. Geosci. Remote Sens.*, vol. 58, no. 10, pp. 7317–7330, Oct. 2020.

[55] H. Zebker and J. Villasenor, "Decorrelation in interferometric radar echoes," *IEEE Trans. Geosci. Remote Sens.*, vol. 30, no. 5, pp. 950–959, May 1992.

[56] R. F. Hanssen, *Radar Interferometry: Data Interpretation and Error Analysis*, vol. 2. Berlin, Germany: Springer, 2001.

[57] F. Gatelli et al., "The wavenumber shift in SAR interferometry," *IEEE Trans. Geosci. Remote Sens.*, vol. 32, no. 4, pp. 855–865, Jul. 1994.

[58] S. Cloude and K. Papathanassiou, "Polarimetric SAR interferometry," *IEEE Trans. Geosci. Remote Sens.*, vol. 36, no. 5, pp. 1551–1565, Sep. 1998.

[59] S. Cloude, *Polarisation: Applications in remote sensing*. Oxford, U.K.: OUP, 2009.

[60] S. Leinss, A. Wiesmann, J. Lemmetyinen, and I. Hajnsek, "Snow Water Equivalent of Dry Snow Measured by Differential Interferometry," *IEEE J. Sel. Topics Appl. Earth Observ. Remote Sens.*, vol. 8, no. 8, pp. 3773–3790, Aug. 2015.

[61] A. Mavrovic, R. Pardo Lara, A. Berg, F. Demontoux, A. Royer, and A. Roy, “Soil dielectric characterization during freeze–thaw transitions using L-band coaxial and soil moisture probes,” *Hydrol. Earth Syst. Sci.*, vol. 25, no. 3, pp. 1117–1131, Mar. 2021.

[62] M. C. Dobson, F. T. Ulaby, M. T. Hallikainen, and M. A. El-Rayes, “Microwave dielectric behavior of wet soil-part II: Dielectric mixing models,” *IEEE Trans. Geosci. Remote Sens.*, vol. GE-23, no. 1, pp. 35–46, Jan. 1985.

[63] L. Zhang, T. Zhao, L. Jiang, and S. Zhao, “Estimate of phase transition water content in freeze–thaw process using microwave radiometer,” *IEEE Trans. Geosci. Remote Sens.*, vol. 48, no. 12, pp. 4248–4255, Dec. 2010.

[64] V. L. Mironov, R. D. De Roo, and I. V. Savin, “Temperature-dependable microwave dielectric model for an Arctic soil,” *IEEE Trans. Geosci. Remote Sens.*, vol. 48, no. 6, pp. 2544–2556, Jun. 2010.

[65] F. Ulaby, *Microwave Radar and Radiometric Remote Sensing*. Ann Arbor, MI, USA: University of Michigan Press, 2014.

[66] J. Boike, F. Miesner, N. Bornemann, W. L. Cable, and I. Grünberg, “Trail Valley Creek, NWT, Canada Soil Moisture and Temperature,” *et seq [dataset publication series]*. PANGAEA, 2023. [Online]. Available: https://doi.org/10.1594/PANGAEA.962726

[67] F. T. Ulaby, W. H. Stiles, and M. Abdelrazik, “Snowcover influence on backscattering from terrain,” *IEEE Trans. Geosci. Remote Sens.*, vol. GE-22, no. 2, no. 2, pp. 126–133, Mar. 1984.

[68] M. Davidson et al., “Copernicus L-band SAR mission requirements document,” *Eur. Space Agency*, Paris, France, ESA-EOPSM-CLIS-MRD-3371, Tech. Rep, 2019.

[69] K. Kellogg et al., “NASA-ISRO Synthetic Aperture Radar (NISAR) mission,” in *Proc. IEEE Aerosp. Conf.*, 2020, pp. 1–21.

Paloma Saporta received the engineering diploma in mechanical engineering from the Ecole nationale des ponts et chaussées, Champs-sur-Marne, France, together with the M. Sc. degree in earth oriented space science and technology from the Technical University of Munich, Munich, Germany, in 2020. She is currently working toward the Ph.D. degree in environmental engineering with the Swiss Federal Institute of Technology (ETH Zurich), Zurich, Switzerland.

Her master thesis was carried out with the Remote Sensing Technology Institute, German Aerospace Center (DLR), Cologne, Germany. In 2021, she joined the Polarimetric SAR Interferometry Research Group, Microwaves and Radar Institute, DLR, Germany. Her main research interests include theory and applications of SAR polarimetry and SAR interferometry, in particular for the characterisation of permafrost landscapes.

Alberto Alonso-González (Member, IEEE) received the B.Sc. degree in computer science, the M.Sc. degree in telecommunication engineering, and the Ph.D. degree from the Technical University of Catalonia (UPC), Barcelona, Spain, in 2007, 2009, and 2014, respectively.

From 2009 to 2014, he was with the Department of Signal Theory and Communications, UPC. From 2014 to 2022, he was with the Microwaves and Radar Institute, German Aerospace Center (DLR), Wessling, Germany, as a member of the Polarimetric synthetic aperture radar (SAR) Interferometry Research Group. Since 2022, he has been with the CommSensLab Group, Department of Signal Theory and Communications, UPC. His research interests include multidimensional SAR, SAR polarimetry and interferometry, digital signal and image processing, remote sensing data modeling, and machine learning techniques applied to agricultural and forest monitoring for climate change mitigation.

Dr. Alonso-González was the recipient of the First Place Student Paper Award at the EUSAR 2012 Conference and the Extraordinary Doctoral Thesis Award from the Technical University of Catalonia in 2016.

Jennika Hammar received the B.Sc. degree in geoecology from the University of Potsdam, Potsdam, Germany, in 2017 and the second B.Sc. degree in remote sensing, geoinformation, and visualization in 2021.

Since then, she has been a Research Associate with the Alfred Wegener Institute, Helmholtz Centre for Polar and Marine Research, Potsdam. Her research interests include observation of permafrost regions using airborne and satellite remote sensing, with a particular emphasis on the drivers of permafrost degradation.

Inge Grünberg received the diploma in hydrology from the Technische Universität Dresden, Dresden, Germany in 2011, and the Ph.D. degree in environmental sciences from the University of Zürich, Zürich, Switzerland, in 2016, where she specialized in permafrost energy balance and radiation fluxes.

Since 2017, she has been a Postdoctoral Scientist with AWI Potsdam, Potsdam, Germany, focusing on the interactions between permafrost soil conditions, climate, and vegetation. Her research interests include field measurements, long-term time series, airborne remote sensing, snow and freeze-thaw processes.

Julia Boike received the M.A. degree in geography, on the topic of “Seasonal hydrology and geochemistry of two small high arctic catchments, Axel Heiberg Island, N.W.T.,” from Wilfrid Laurier University, Waterloo, ON, Canada, in 1993, and the Ph.D. degree in mineralogy, on the topic of “Thermal, hydrological and geochemical dynamics of the active layer, Siberia,” from the Institute for Geosciences, University of Potsdam, Potsdam, Germany, in 1997.

During 2000–2003, she conducted postdoctoral work through a Leopoldina stipend at the Water and Environmental Research Center, University of Alaska, Fairbanks, AK, USA. During 2006–2016, she was the Leader of the Helmholtz Young Investigators Research Group on “Sensitivity of the permafrost system’s water and energy balance under changing climate: A multiscale perspective” hosted by the Periglacial Section at the Alfred Wegener Institute, Potsdam and the Institute for Environmental Physics, University of Heidelberg, Heidelberg, Germany. She was a Cocoordinator of the large-scale EU project Changing Permafrost in the Arctic and Its Global Effects in the 21st Century (PAGE21). She is currently a Senior Group Leader with the Alfred Wegener Helmholtz Institute and a Private Docent with the University of Heidelberg. Her experience includes more than 25 years of Arctic experimental research at permafrost sites in Canada, Svalbard, Siberia, and Alaska. Her research interests include thermal, hydrological, and biogeochemical processes and land–atmosphere observations and modeling in northern permafrost areas.

Dr. Boike is a Member of the American Geophysical Union and the European Geophysical Union. She was the recipient of the First Annual Award for Arctic Research Excellence of the Arctic Research Consortium of the United States (1997) and the Horton Hydrology Research Grant of the American Geophysical Union (1995). She is an expert in the Global Cryosphere Watch working structure of the World Meteorological Organization.

Irena Hajnsek (Fellow, IEEE) received the Dipl. degree in the topic of fluvial river systems (Honors) from the Free University of Berlin, Berlin, Germany, in 1996, and the Dr. rer. nat. degree (Honors) in model-based estimation of soil moisture from fully polarimetric Synthetic Aperture Radar in 2001 from the Friedrich Schiller University of Jena, Jena, Germany, in 2001.

Since November 2009, she has been a Professor of Earth Observation with the Swiss Federal Institute of Technology (ETH), Zürich Institute of Environmental Engineering, Zurich, Switzerland, and the Head of the Polarimetric SAR Interferometry Research Group with the German Aerospace Center Microwaves and Radar Institute. Her main research interests include electromagnetic propagation and scattering theory, radar polarimetry, SAR and interferometric SAR data processing techniques, environmental parameter modelling and estimation.

Prof. Hajnsek has been the recipient of the Doctor degree honoris causa from the University of Oslo, Oslo, Norway, in 2024, for her outstanding contributions to science, including the development of algorithms using innovative radar techniques for environmental parameter estimation and setting requirements for the design of future radar missions in application areas as permafrost, glaciers, disaster management, agriculture, and climate change impacts. Since 2010, she has been the Science Coordinator of the German satellite mission TanDEM-X. Currently, she is a Member of the European Space Agency Mission Advisory Group for the ROSE-L Mission. She was Technical Program Co-chair of the IEEE IGARSS 2012 in Munich, Germany and 2019 in Yokohama, Japan. From 2013 to 2021 she was a Member of the IEEE GRSS AdCom and from 2016 to 2020 the Vice President of the IEEE GRSS Technical Committees. She is the founder of the new Technical Committee Remote Sensing Environment, Analysis, and Climate Technologies that exists since Nov 2021.